

1 **Resupply of mesopelagic dissolved iron controlled by particulate iron composition**

2

3 M. Bressac^{1,2,*}, C. Guieu^{2,3}, M. J. Ellwood⁴, A. Tagliabue⁵, T. Wagener⁶, E. C. Laurenceau-
4 Cornec¹, H. Whitby⁷, G. Sarthou⁷, P. W. Boyd^{1,8}

5

6 ¹ Institute for Marine and Antarctic Studies, University of Tasmania, Hobart, Tasmania,
7 Australia

8 ² Sorbonne Université, CNRS, Laboratoire d'Océanographie de Villefranche, LOV, F-06230,
9 Villefranche-sur-mer, France

10 ³ The Center for Prototype Climate Modeling, New York University in Abu Dhabi, Abu
11 Dhabi, UAE

12 ⁴ Research School of Earth Sciences, Australian National University, Canberra, ACT,
13 Australia

14 ⁵ Department of Earth Ocean and Ecological Sciences, School of Environmental Sciences,
15 University of Liverpool, Liverpool, UK

16 ⁶ Aix Marseille Univ, CNRS, IRD, Université de Toulon, MIO UM 110, 13288, Marseille,
17 France

18 ⁷ UMR 6539/LEMAR/IUEM, CNRS, UBO, IRD, Ifremer, Technopôle Brest Iroise, Place
19 Nicolas Copernic, 29280 Plouzané, France

20 ⁸ Antarctic Climate and Ecosystems Collaborative Research Center, University of Tasmania,
21 Hobart, Tasmania, Australia

22 * Communicating author: matthieu.bressac@utas.edu.au

23

24 **Dissolved iron supply controls half of ocean primary productivity. Resupply by**
25 **remineralization of sinking particles, and subsequent vertical mixing, largely sustains**

26 **this productivity. However, our understanding of the drivers of dissolved iron resupply,**
27 **and their influence on its vertical distribution across the oceans, is still limited due to**
28 **sparse observations. There is a lack of empirical evidence for what controls subsurface**
29 **iron remineralization due to difficulties in studying mesopelagic biogeochemistry. Here,**
30 **we present estimates of particulate transformations to dissolved iron, concurrent oxygen**
31 **consumption and iron-binding ligand replenishment based on *in situ* mesopelagic**
32 **experiments. Dissolved iron regeneration efficiencies (i.e., replenishment/oxygen**
33 **consumption) were ten- to one hundred-fold higher in low-dust Subantarctic waters**
34 **relative to higher-dust Mediterranean sites. Regeneration efficiencies are heavily**
35 **influenced by particle composition. Their make-up dictates ligand release, controls**
36 **scavenging, modulates ballasting, and may lead to differential remineralization of**
37 **biogenic versus lithogenic iron. At high-dust sites these processes together increase the**
38 **iron remineralization length-scale. Modelling reveals that in oceanic regions near**
39 **deserts, enhanced lithogenic fluxes deepen the ferricline, which alter vertical patterns of**
40 **dissolved iron replenishment, and set its redistribution at the global scale. Such wide-**
41 **ranging regeneration efficiencies drive different vertical patterns in dissolved iron**
42 **replenishment across oceanic provinces.**

43

44 Globally, the productivity of major phytoplankton groups, including diatoms and diazotrophs,
45 is set by dissolved iron (DFe) supply¹. Twenty years of research has revealed diverse modes
46 of DFe supply, from dust to hydrothermal vents, and their regional influences^{2,3}. Iron
47 biogeochemistry is a rapidly evolving field, driving the development of global modelling
48 initiatives⁴. However, iron cycling in the oceans' interior, a fundamental component of iron
49 biogeochemistry^{5,6}, represents a major unknown, and critically is hindering model
50 development⁷.

51

52 Deep winter mixing is a key vector in the annual resupply of upper ocean DFe stocks⁸. At
53 depth, DFe is replenished via biotic (e.g., microbial solubilization) and abiotic (e.g.,
54 dissolution) transformations (also termed remineralization or replenishment here) of
55 particulate Fe (PFe)⁷. To date, internal iron cycling has been investigated using three
56 distinctive approaches, each of which has improved its representation in biogeochemical
57 models⁹⁻¹¹. Firstly, studies deploying trace metal-clean multi-depth sediment traps, in regions
58 dominated by biogenic PFe, provided initial evidence of subsurface decoupling in PFe
59 remineralization relative to phosphorus (P), carbon (C) or nitrogen¹²⁻¹⁵. Second, bacterially-
60 mediated PFe remineralization – suppressed in sediment trap studies due to preservatives –
61 was investigated in shipboard time-series incubations of resuspended mesopelagic particles in
62 which the release of DFe and Fe-binding ligands resulted from particle degradation^{9,16}. Third,
63 dust addition experiments within nearshore 15 m deep mesocosms demonstrated that
64 lithogenic Fe, conventionally viewed as a major source of external Fe to surface waters^{1,2,17},
65 can either release (dissolution) or remove (scavenging) DFe depending on the initial
66 biogeochemical conditions¹⁸⁻²⁰.

67

68 These three approaches to internal iron cycling targeted different processes, such as ligand
69 and DFe release^{9,16}, patterns in PFe flux attenuation¹²⁻¹⁵, or scavenging and dissolution¹⁸⁻²⁰.
70 However, it is difficult to compare the findings of these studies as they each sampled particle
71 assemblages with differing contributions from biogenic and lithogenic iron. Hence, no study
72 so far has examined the relative role of the different processes associated with biogenic versus
73 lithogenic Fe on internal iron cycling. The hypothesis⁹ that the composition of particles will
74 largely determine mesopelagic patterns of DFe replenishment remains untested due to
75 difficulties in studying this stratum²¹ and in discriminating between biogenic and lithogenic

76 PFe within sinking particles⁷. Here, we overcame both limitations by targeting regions
77 dominated by biogenic, a mix of biogenic/lithogenic, or lithogenic sinking PFe, and applying
78 a novel *in situ* particle interceptor/incubator – RESPIRE²² – to iron biogeochemistry to
79 concurrently elucidate the roles of biogenic and lithogenic PFe and their fate within the upper
80 mesopelagic zone (~100-200 m depth).

81

82 **Contrasting biogeochemical areas** – Mesopelagic Fe cycling was studied using a trace
83 metal-clean version of RESPIRE (TM-RESPIRE; Supplementary-Fig. 1) on a surface-
84 tethered free-drifting mooring to non-intrusively intercept settling particles, and then
85 immediately (i.e., at the end of the 1-2 d collection period) incubate them within this device at
86 *in situ* pressure and temperature. RESPIRE²² provides rates of remineralization by particle-
87 attached bacteria based on an oxygen consumption time-series (Fig. 1a-b). TM-RESPIRE
88 provides the PFe/P/C sinking fluxes and associated DFe/P/C replenishment rates along with
89 concurrent release of iron-binding ligands. In doing so, the TM-RESPIRE approach (along
90 with subsequent analysis to estimate scavenging) combines all three previous approaches and
91 permits the investigation *in situ* of the different processes driving the Fe remineralization and
92 their interplay.

93

94 RESPIRE and TM-RESPIRE were deployed (vertically separated by <20 m; Methods) at 1 or
95 2 depths in the upper mesopelagic (110-200 m depth) during GEOTRACES process studies in
96 the Subantarctic Zone (SAZ) and Mediterranean Sea (Supplementary-Table 1; Methods).
97 These sites span wide-ranging dust deposition and productivity regimes (Fig. 1c). At SAZ,
98 High-Nitrate-Low-Chlorophyll (HNLC) surface waters are characterized by low dust
99 deposition and biologically-limiting DFe levels²⁴. In contrast, Fe-rich oligotrophic waters of
100 the Eastern Mediterranean (ION site) encounter intense Saharan dust deposition event²³. In

101 addition, a site within the Algerian basin (Western Mediterranean, ALG site) was selected
102 since it had intermediate characteristics between these end-members (Fig. 1c).

103

104 These site-specific characteristics were reflected in the widely-differing particulate organic
105 carbon (POC) and PFe sinking fluxes (Fig. 2; Supplementary-Table 1). SAZ had low POC
106 fluxes ($0.9\text{-}1.2\text{ mmol m}^{-2}\text{ d}^{-1}$), but in contrast to the seasonal biological trends evident in Fig.
107 1c, ~ 4 -fold higher POC fluxes were measured at ION and ALG relative to SAZ, suggesting
108 that a higher proportion of productivity was exported at these higher dust sites. This trend was
109 probably due to lithogenic ballasting which is often associated with a high proportion of the
110 POC export in the Mediterranean Sea^{25,26}. PFe fluxes at the Mediterranean sites were also
111 ~ 15 -fold higher ($8.0\text{-}12.5\text{ }\mu\text{mol m}^{-2}\text{ d}^{-1}$ at 115 m depth) relative to the Subantarctic. This
112 order-of-magnitude difference was driven by dust-derived lithogenic material
113 (Supplementary-Fig. 2b and f), a major constituent of Mediterranean sinking fluxes²⁶ but
114 negligible at SAZ²⁷. Indeed, the Fe/C ratio of the sinking particles, a proxy of the
115 biogenic:lithogenic PFe (Methods), ranged >30 -fold ($\sim 460\text{-}13970\text{ }\mu\text{mol/mol}$) confirming the
116 SAZ site as the low lithogenic Fe end member (Fig. 3b-c). At ALG and ION, contrasting POC
117 and PFe flux attenuation patterns were evident, with PFe increasing with depth while a 3-fold
118 attenuation of POC flux occurred between 115-195 m depth (Fig. 2). Consequently, a
119 decrease in the relative proportion of biogenic PFe occurred over this stratum, evident by
120 increased Fe/C ratios (Fig. 3b-c).

121

122 **Mesopelagic bacterial remineralization** – Oxygen-based remineralization rates were
123 correlated linearly to the POC concentrations within the RESPIRE (i.e., the intercepted POC
124 flux; Fig. 3a). The absence of significant relationship(s) with other flux characteristics
125 (Supplementary-Fig. 2a-d), reveals that POC exerted a first-order control on remineralization

126 rates. To assess whether DFe replenishment is largely driven by microbial solubilization of
127 biogenic Fe in settling particles, we investigated trends in Fe regeneration efficiency (R_{Fe/O_2}).
128 Both site-specific and water-column processes contributed to the wide range of R_{Fe/O_2} (Fig.
129 3b). High R_{Fe/O_2} efficiencies were observed at the SAZ site (148-421 $\mu\text{mol}/\text{mol}$) but were one-
130 to two-orders of magnitude lower at both Mediterranean sites. These trends in R_{Fe/O_2} are
131 consistent with vertical DFe stocks increasing with depth at SAZ, and in contrast decreasing
132 at the Mediterranean sites (Supplementary-Fig. 3). Similarly, replenishment rates of P and C
133 were highest at SAZ (Supplementary-Table 2). Although the present study offers a snapshot
134 of the annual cycle of mesopelagic remineralization, our observations are consistent with
135 high-latitude studies characterized as sites with relatively labile particles prone to microbially-
136 mediated remineralization^{28,29}.

137

138 Despite the complex transformations that characterize the internal cycle of Fe, a strong
139 inverse relationship is observed between R_{Fe/O_2} and the composition of the PFe flux estimated
140 from the particulate Fe/C ratio (Fig. 3b). Critically, this inverse relationship reveals that R_{Fe/O_2}
141 is not determined by the magnitude of the PFe flux but rather by its particle composition
142 (Supplementary-Fig. 2g-h). Furthermore, this negative relationship strongly suggests that
143 biogenic PFe is efficiently regenerated while the dissolution of lithogenic PFe (predominant
144 at the Mediterranean sites; Fig. 2) takes place at much lower rates, corroborating 1D model
145 simulations showing that biogenic and lithogenic PFe fluxes exhibit distinctly different
146 vertical attenuation⁹.

147

148 **Drivers of mesopelagic iron remineralization** – To develop a better understanding of the
149 drivers of mesopelagic iron biogeochemistry, R_{Fe/O_2} was converted into a Fe/C regeneration
150 ratio ($R_{\text{Fe}/\text{C}}$; Methods) and compared with the Fe/C and biogenic Fe/C ($\text{Fe}_{\text{bio}}/\text{C}$)

151 stoichiometries of the intercepted particles (Fig. 3c). A positive linear relationship (i.e.,
152 similar biogenic flux and regenerative stoichiometries) should be observed if bacterial
153 solubilization exerts a first-order control on DFe resupply. Here, the absence of such a
154 relationship, along with systematically lower DFe replenishment rates relative to P and C
155 (Supplementary-Table 2), confirm that DFe resupply results from a combination of biotic and
156 abiotic transformations of sinking PFe^{15,17}. As highlighted in Fig. 3c, dissolution of lithogenic
157 Fe (i.e., DFe release without O₂ consumption) increases R_{Fe/O_2} and hence $R_{\text{Fe}/\text{C}}$, whereas Fe
158 scavenging (i.e., DFe removal without O₂ consumption) has the opposite effect. As expected
159 for areas dominated by biogenic PFe such as the subantarctic, bacterial solubilization
160 explained most of the $R_{\text{Fe}/\text{C}}$ relative to that of scavenging (Fig. 3c). The relatively large excess
161 in post-incubation Fe-binding ligands (L*) observed at SAZ (Fig. 4), driven by bacterial
162 degradation of biogenic-dominated sinking particles^{9,16}, is consistent with these low
163 scavenging rates pointing to complex interplay between processes associated with biogenic
164 and lithogenic PFe.

165

166 In contrast, a pronounced mismatch was observed between $R_{\text{Fe}/\text{C}}$ and the biogenic flux
167 stoichiometry at ALG at the deeper depth (195 m) and both depths at ION (Fig. 3c). Although
168 this trend results from the dominance of particle scavenging over solubilization/dissolution
169 (Fig. 4), the increase of this mismatch with depth may be explained by increasing scavenging
170 and/or decreasing solubilization/dissolution. Saharan dust-derived Fe dissolution rates are
171 reported to remain constant for several days in lab-studies³⁰, arguing for a relatively constant
172 dissolution rate over this 115-195 m stratum that particles will sink through on this
173 timescale^{7,9}. Although changes in the bacterial solubilization rate of PFe, over this depth
174 range, cannot be directly assessed, the increasing proportion of C respired with depth
175 (Supplementary-Table 2) is not consistent with decreased bacterial solubilization rate of PFe

176 (by assuming constant or increasing biogenic Fe/C ratio¹⁵). Thus, increased scavenging (Fig.
177 4), is the most likely mechanism to account for the trend in $R_{\text{Fe/C}}$ with depth.

178

179 Measurements of size and concentration of particles collected at the Mediterranean sites
180 revealed decreasing cumulative particle volume concentrations with depth (Supplementary-
181 Table 4), excluding these two parameters as possible drivers of increased scavenging rate.
182 Therefore, the increase with depth in the relative proportion of lithogenic material being
183 exported (Supplementary-Fig. 2b and f), and the resulting decrease in the release of Fe-
184 binding ligands (Supplementary-Table 3), are most likely jointly responsible for this shift
185 within the upper mesopelagic (115-195 m; ALG/ION) stratum in the balance between
186 remineralization of biogenic PFe (DFe and ligand release), dissolution of lithogenic PFe (DFe
187 release) and scavenging processes. These findings demonstrate the confounding role played
188 by dust-derived lithogenic particles, conventionally viewed as a major pelagic DFe source^{2,5},
189 but shown here in the upper 100-200 m stratum to act primarily as a scavenging-modulated
190 sink for DFe, and as a ballasting agent^{25,31,32}, each influencing where in the water column DFe
191 is replenished.

192

193 **Vertical resetting of mesopelagic biogeochemical conditions** – Figure 4 summarises how
194 the interplay of biogenic and lithogenic processes establish iron biogeochemical conditions at
195 each site, and importantly reset conditions with depth. Biogenic PFe is the main source of
196 DFe replenishment via bacterial solubilization, and this is also the case for the concurrent
197 release of iron-binding ligands. By combining the observations from TM-RESPIRE with
198 dissolution rate and scavenging ratios derived from prior dust-addition studies^{18,30}, it is
199 evident that lithogenic PFe contributes ~10 times more to Fe scavenging relative to Fe
200 dissolution in the upper mesopelagic (Fig. 4) supporting our observations in Fig. 3c. It is

201 important to note that high scavenging rates were reported even when L^* was (slightly)
202 positive (Fig. 3c and 4). It is probable that the higher the value of L^* the less likelihood of
203 pronounced scavenging, however, this trend, of scavenging when L^* is positive, points to an
204 unknown or unexplored mechanism (e.g., sorption of complexed Fe, colloidal aggregation).
205 These contrasting biogenic and lithogenic roles point to the importance of the composition of
206 the PFe flux in setting the Fe remineralization length-scale, with high PFe attenuation at the
207 biogenic end-member site, and in contrast an increase in PFe sinking flux at the lithogenic
208 end-member site.

209

210 Conceptually, depth-dependant changes in the relative proportion of biogenic vs. lithogenic
211 PFe, driven by their different attenuation length-scales, result in an ongoing resetting of the
212 biogeochemical conditions (e.g., L^* , ballasting via changes to the specific gravity of the
213 particle) while particles are settling in the water column (Fig. 4). The vertical trend observed
214 at the ALG site – characterized by intermediate surface characteristics relative to the two
215 other sites (Fig. 1c) – illustrates this dynamic situation. At 115 m depth, bacterial degradation
216 of heterogenous (i.e., biogenic/lithogenic) particles resulted in a relatively high post-
217 incubation L^* (Fig. 4) and a low scavenging rate (Fig. 3c and 4). However, 80 m deeper,
218 alteration of the composition of the PFe flux resulted in a decrease in post-incubation L^* (Fig.
219 4; Supplementary-Table 3) and a marked increase in the scavenging rate (Fig. 3c and 4). A
220 similar increase in scavenging with depth was observed at the ION site (Fig. 4). The dynamic
221 interplay between biogenically- and lithogenically-modulated mechanisms explain the
222 unexpected high spatial (and by analogy, temporal) and vertical variability in the PFe
223 remineralization reported in this study, but not so far captured in biogeochemical models⁷.

224

225 We report a ~thousand-fold range in the DFe replenishment rate, while only modest changes
226 in P and C remineralization rates occurred at all sites (Supplementary-Table 2). At the SAZ,
227 the decoupling between Fe and C remineralization was relatively low and comparable to that
228 reported for sinking diatoms in subtropical waters¹⁵. In contrast, a pronounced decoupling
229 between Fe and both C and P remineralization was observed at ALG and ION. Critically, the
230 lithogenic component of the sinking flux, by having virtually no influence on C and P
231 remineralization, amplifies the decoupling between the Fe and both the C and P
232 remineralization length-scales. This finding highlights that the multi-faceted effects of particle
233 composition and dynamics on mesopelagic iron recycling needs to be considered in global
234 biogeochemical models, to better explain the spatial variability in the decoupling of nutrient
235 recycling.

236

237 **Controls on the global iron distribution** – The most straightforward route to examining the
238 broader role of biogenic:lithogenic particle composition on iron distributions was to focus on
239 the links to lithogenic iron, as dust supply is a well-established component of iron
240 biogeochemical models⁴. The modelling simulations exploited the observed Fe/O₂
241 relationship with dust (Fig. 3b-c) to develop a simple first-order parameterization that
242 captures observed links between Fe/O₂ and dust (Fig. 5a). Thus, an additional modulator of Fe
243 remineralization, based on the atmospherically-derived lithogenic particle concentration, was
244 added to the PISCES model parameterization, which enabled the sensitivity of iron
245 biogeochemistry to the impact of lithogenic particles on mesopelagic DFe cycling to be
246 addressed (Methods).

247

248 This simulation was employed to assess the wider implications of the multi-faceted roles of
249 lithogenic Fe on ocean iron cycling. Projections of the upper mesopelagic (100-250 m) DFe

250 inventory, in this amended simulation, decreased by 23.7% relative to the control run (Fig.
251 5b) and as expected, this trend was especially marked in areas influenced by high dust
252 deposition (i.e., North Atlantic, North Pacific, and Indian Oceans). In parallel, the DFe
253 inventory between 1000-1250 m depth increased by 6.4% across the global ocean (Fig. 5b).
254 Ultimately, the effect of lithogenic particles on PFe remineralization is to deepen the vertical
255 profile of DFe and therefore drive the replenishment of DFe deeper in the water column (Fig.
256 5c). This significant redistribution of DFe over the upper 1000 m has important ramifications
257 when considering that this depth stratum is heavily influenced by mode and intermediate
258 waters lateral transport³³, which can then alter DFe supply to different ocean regions and the
259 associated primary production (Supplementary-Fig. 4b). Therefore, the vertical redistribution
260 of iron in regions dominated by settling lithogenic particles may be pronounced when changes
261 in dust delivery to the ocean³⁴ may be accompanied by altered ocean circulation in the coming
262 decades⁵.

263

264 Our findings suggest that predicted changes in dust inputs³⁴, by altering the
265 biogenic:lithogenic composition of the sinking particle assemblage, may impact the
266 replenishment of the subsurface DFe inventory and vertical supply of DFe not only in dusty
267 regions, but across the global ocean. This alteration, across many oceanic provinces, of DFe
268 resupply may in return have profound effects on the carbon sequestration efficiency of the
269 biological pump³⁵. Our study enhances the wider understanding of the role of dust in altering
270 particle composition which in turn influences the replenishment of the subsurface DFe
271 inventory. This research points to the need for further studies on the internal cycling of trace
272 metals if we are to fully understand how they are returned to surface waters via their
273 biogeochemical cycles.

274

275 **References**

- 276 1. Moore, C. M. *et al.* Processes and patterns of oceanic nutrient limitation. *Nat. Geosci.* **6**,
277 701-710 (2013).
- 278 2. Jickells, T. D. *et al.* Global iron connections between desert dust, ocean biogeochemistry,
279 and climate. *Science* **308**, 67-71 (2005).
- 280 3. Guieu, C., *et al.* Iron from a submarine source impacts the productive layer of the Western
281 Tropical South Pacific (WTSP). *Sci. Rep.* **8**, 9075 (2018).
- 282 4. Tagliabue, A. *et al.* How well do global ocean biogeochemistry models simulate dissolved
283 iron distributions? *Glob. Biogeochem. Cycles* **30**, 149-174 (2016).
- 284 5. Tagliabue, A. *et al.* The integral role of iron in ocean biogeochemistry. *Nature* **543**, 51-59
285 (2017).
- 286 6. GEOTRACES Planning Group. GEOTRACES Science Plan. Baltimore, Maryland:
287 Scientific Committee on Oceanic Research (2006).
- 288 7. Boyd, P. W., Ellwood, M. J., Tagliabue, A., & Twining, B. S. Biotic and abiotic retention,
289 recycling and remineralization of metals in the ocean. *Nat. Geosci.* **10**, 167-173 (2017).
- 290 8. Tagliabue, A. *et al.* Surface-water iron supplies in the Southern Ocean sustained by deep
291 winter mixing. *Nat. Geosci.* **7**, 314-320 (2014).
- 292 9. Boyd, P. W., Iribarren, E., Sander, S. G., Hunter, K. A., & Jackson, G. A.
293 Remineralization of upper ocean particles: Implications for iron biogeochemistry. *Limnol.*
294 *Oceanogr.* **55**, 1271-1288 (2010).
- 295 10. Ye, Y., Wagener, T., Völker, C., Guieu, C., & Wolf-Gladrow, D. A.. Dust deposition: iron
296 source or sink? A case study. *Biogeosciences* **8**, 2107-2124 (2011).
- 297 11. Völker, C., & Tagliabue, A. Modeling organic iron-binding ligands in a three-dimensional
298 biogeochemical ocean model. *Mar. Chem.* **173**, 67-77 (2015).

- 299 12. Frew, R. D. *et al.* Particulate iron dynamics during FeCycle in subantarctic waters
300 southeast of New Zealand. *Glob. Biogeochem. Cycles* **20**, GB1S93 (2006).
- 301 13. Lamborg, C. H., Buesseler, K. O., & Lam, P. J. Sinking fluxes of minor and trace
302 elements in the North Pacific Ocean measured during the VERTIGO program. *Deep Sea*
303 *Res. Part II* **55**, 1564-1577 (2008).
- 304 14. Ellwood, M. J. *et al.* Pelagic iron cycling during the subtropical spring bloom, east of
305 New Zealand. *Mar. Chem.* **160**, 18-33 (2014).
- 306 15. Twining, B. S. *et al.* Differential remineralization of major and trace elements in sinking
307 diatoms. *Limnol. Oceanogr.* **59**, 689-704 (2014).
- 308 16. Velasquez, I. B. *et al.* Ferrioxamine siderophores detected amongst iron binding ligands
309 produced during the remineralization of marine particles. *Front. Mar. Sci.* **3**, 172 (2016).
- 310 17. Boyd, P. W., & Ellwood, M. J. The biogeochemical cycle of iron in the ocean. *Nat.*
311 *Geosci.* **3**, 675-682 (2010).
- 312 18. Wagener, T., Guieu, C., & Leblond, N. Effects of dust deposition on iron cycle in the
313 surface Mediterranean Sea: results from a mesocosm seeding experiment. *Biogeosciences*
314 **7**, 3769-3781 (2010).
- 315 19. Bressac, M., & Guieu, C. Post-depositional processes: What really happens to new
316 atmospheric iron in the ocean's surface? *Glob. Biogeochem. Cycles* **27**, 859-870 (2013).
- 317 20. Wuttig, K. *et al.* Impacts of dust deposition on dissolved trace metal concentrations (Mn,
318 Al and Fe) during a mesocosm experiment. *Biogeosciences* **10**, 2583-2600 (2013).
- 319 21. Burd, A. B. *et al.* Assessing the apparent imbalance between geochemical and
320 biochemical indicators of meso-and bathypelagic biological activity: What the @\$#! is
321 wrong with present calculations of carbon budgets? *Deep Sea Res. Part II* **57**, 1557-1571
322 (2010).

- 323 22. Boyd, P. W., McDonnell, A., Valdez, J., Lefèvre, D., & Gall, M. P. RESPIRE: An in situ
324 particle interceptor to conduct particle remineralization and microbial dynamics studies in
325 the oceans' Twilight Zone. *Limnol. Oceanogr. Methods* **13**, 494-508 (2015).
- 326 23. Albani, S. *et al.* Improved dust representation in the Community Atmosphere Model. *J.*
327 *Adv. Model Earth Sy.* **6**, 541-570 (2014).
- 328 24. Sedwick, P. N., *et al.* Limitation of algal growth by iron deficiency in the Australian
329 Subantarctic region. *Geophys. Res. Lett.* **26**, 2865-2868 (1999).
- 330 25. Bressac, M. *et al.* Quantification of the lithogenic carbon pump following a simulated
331 dust-deposition event in large mesocosms. *Biogeosciences* **11**, 1007-1020 (2014).
- 332 26. Ternon, E. *et al.* The impact of Saharan dust on the particulate export in the water column
333 of the North Western Mediterranean Sea. *Biogeosciences* **7**, 809-826 (2010).
- 334 27. Trull, T. W., Bray, S. G., Manganini, S. J., Honjo, S., & Francois, R. Moored sediment
335 trap measurements of carbon export in the Subantarctic and Polar Frontal Zones of the
336 Southern Ocean, south of Australia. *J. Geophys. Res.* **106**, 31489-31509 (2001).
- 337 28. Francois, R., Honjo, S., Krishfield, R., & Manganini, S. Factors controlling the flux of
338 organic carbon to the bathypelagic zone of the ocean. *Glob. Biogeochem. Cycles* **16**, 34-1
339 (2002).
- 340 29. Henson, S. A., Sanders, R., & Madsen, E. Global patterns in efficiency of particulate
341 organic carbon export and transfer to the deep ocean. *Glob. Biogeochem. Cycles* **26**,
342 GB1028 (2012).
- 343 30. Wagener, T., Pulido-Villena, E., & Guieu, C. Dust iron dissolution in seawater: Results
344 from a one-year time-series in the Mediterranean Sea. *Geophys. Res. Lett.* **35**, L16601
345 (2008).

- 346 31. Louis, J., Pedrotti, M. L., Gazeau, F., & Guieu, C. Experimental evidence of formation of
347 Transparent Exopolymer Particles (TEP) and POC export provoked by dust addition
348 under current and high pCO₂ conditions. *PloS one* **12**, e0171980 (2017).
- 349 32. Pabortsava, K. *et al.* Carbon sequestration in the deep Atlantic enhanced by Saharan dust.
350 *Nat. Geosci.* **10**, 189 (2017).
- 351 33. Hanawa, K. & Talley, L. D. in *Ocean Circulation and Climate*. Eds Siedler, G. & Church,
352 J., Academic, San Diego, 373–386 (2001).
- 353 34. Mahowald, N. M., & Luo, C. A less dusty future?. *Geophys. Res. Lett.* **30**, 1903 (2003).
- 354 35. Blain, S. *et al.* Effect of natural iron fertilization on carbon sequestration in the Southern
355 Ocean. *Nature* **446**, 1070-1074 (2007).

356

357 **Corresponding author** – Correspondence and requests for materials should be addressed to
358 M.B. (matthieu.bressac@utas.edu.au).

359

360 **Acknowledgements** – We thank the captains and crew of the *RV Investigator* and *RV*
361 *Pourquoi Pas?*, the CSIRO and DT INSU teams for the design and preparation of the
362 mooring line, C. Young and P. Waller for building the TM-RESPIRE. The CSIRO
363 Hydrochemistry team, S. Albani, N. Bhairy, E. Cavan, X. Chan, G. De Liège, J. Derrick, K.
364 Desboeufs, F. D’Ortenzio, A. Dufour, M. Garel, J. Guittonneau, N. Haentjens, S. Helias
365 Nunige, S. Jacquet, P. Jansen, N. Leblond, D. Lefèvre, H. Planquette, C. Ridame, G. Rougier,
366 V. Tallendier, C. Tamburini, A. Tovar-Sanchez and T. Trull are thanked for their help at sea
367 and/or samples analysis. This project was funded by a Marie Skłodowska-Curie Postdoctoral
368 European Fellowship awarded to M.B (European Union Seventh Framework Programme
369 ([FP7/2007-2013]) under grant agreement no. [PIOF-GA-2012-626734] (IRON-IC project)).
370 This study is a contribution to the PEACETIME project (<http://peacetime-project.org>), a joint

371 initiative of the MERMEX and ChArMEx components supported by CNRS-INSU,
372 IFREMER, CEA, and Météo-France as part of the programme MISTRALS coordinated by
373 INSU. This study was also partly funded by the Australian Research Council by a Laureate
374 awarded to P.W.B (FL160100131), and Discovery project awarded to M.J.E and P.W.B.
375 (DP170102108).

376

377 **Author contributions** – M.B. designed and carried out the study, analysed the data, and
378 wrote the manuscript. C.G. and P.W.B. helped in the design of the study and co-led the
379 cruises. P.W.B. worked on the different versions of the manuscript. M.J.E., T.W., and
380 E.C.L.C. helped in the different instrument deployments and sampling. M.J.E., and T.W.
381 helped in the analysis of samples. A.T. provided and helped interpret the PISCES model
382 output. H.W. and G.S. analyzed the ligand samples. All authors commented on and
383 contributed to the improvement of the manuscript.

384

385 **Competing interests** – The authors declare no competing interests.

386

387 **Figure 1. *In situ* particle remineralization measurements at contrasting biogeochemical**
388 **sites. a,** Conceptual alteration of particles within the (TM-)RESPIRE. Sinking particles are
389 intercepted for ~36h and regularly transferred into the inner chamber. Next, particles are
390 immediately incubated for >24h at *in situ* pressure and temperature during which bacterial
391 solubilization (i.e., diminished green particles) releases elements. See Methods for chemical
392 assays, and corrections applied to obtain pre-incubation particulate concentrations. **b,** Typical
393 oxygen optode time-series measured within RESPIRE. Bacterially-mediated remineralization
394 is derived from ΔO_{2max} and Δt (i.e., the time-period where the slope of the linear regression is
395 maximum). **c,** Weekly chlorophyll climatology from Modis-Aqua (green; 2003–2017; $1^\circ \times 1^\circ$

396 resolution) and monthly climatology of simulated dust deposition (brown; $0.9^\circ \times 1.25^\circ$
397 resolution)²³ in the subantarctic (SAZ: upper-panel), and Mediterranean Sea (ALG: middle;
398 ION: lower-panel). Grey vertical bars are (TM-)RESPIRE sampling periods.

399

400 **Figure 2. Summary of downward particle fluxes and composition from (TM-)RESPIRE**
401 **at SAZ (green), ALG (red) and ION (blue).** Coloured solid circles denote POC fluxes
402 ($\text{mmol m}^{-2} \text{d}^{-1}$; averaged (TM-)RESPIRE fluxes) at each depth (left-hand downward arrow,
403 corresponding to the centre of each circle). PFe fluxes ($\mu\text{mol m}^{-2} \text{d}^{-1}$) are represented by
404 coloured circle rims, and the partitioning of the PFe flux by the proportion of grey
405 (lithogenic) and white (biogenic) within each circle (Methods). All fluxes were corrected for
406 bacterial remineralization during the incubation (Methods). The circle size represents the flux
407 magnitude (Supplementary-Table 1) and are enlarged 10-fold (inside the dashed rectangle) at
408 the low-flux SAZ site. At SAZ, fluxes are the mean of two successive deployments (same
409 depth).

410

411 **Figure 3. Bacterial particle remineralization and iron regeneration efficiency at SAZ**
412 **(green), ALG (red) and ION (blue).** **a,** Remineralization versus POC concentrations
413 (corrected for remineralization during the incubation) measured within RESPIRE at 115 m
414 (triangles), 160 m (circles), and 195 m (diamonds). The best-fit of the linear model is plotted.
415 **b,** Regeneration efficiencies (R_{Fe/O_2}) versus the Fe/C molar ratios of intercepted particles (a
416 proxy for PFe flux composition, higher ratios have more $\text{PFe}_{\text{litho}}$; Methods). The best-fit of the
417 power law model is presented. **c,** Fe/C regeneration ratios ($R_{\text{Fe}/\text{C}}$), obtained from R_{Fe/O_2} and a
418 C:O₂ conversion factor (Methods), versus the bulk (open symbols) and biogenic ($\text{Fe}_{\text{bio}}/\text{C}$;
419 Methods; closed symbols) Fe/C molar ratios. To aid interpretation, Fe-specific processes
420 (vertical arrows) in relation to $R_{\text{Fe}/\text{C}}$ and $\text{Fe}_{\text{bio}}/\text{C}$ are displayed. The grey triangle illustrates the

421 increasing proportion of lithogenic PFe across sites and with depth. Error bars were derived
422 using uncertainty-propagation laws (Methods). Fluxes were expressed as concentrations to
423 permit cross-comparison between sites (different collection/incubation times employed).

424

425 **Figure 4. Synthesis of key processes that together set the PFe remineralization length-**
426 **scale expressed as a function of the relative proportion of sinking biogenic:lithogenic**
427 **PFe.** Sites and depths are assigned into each of three idealized categories: biogenic-dominated
428 (SAZ), heterogeneous (biogenic/lithogenic; ALG 115 m), and lithogenic-dominated (ALG
429 195 m, ION 115-195 m) PFe fluxes. Note, how intercepted sinking particles at ALG shift
430 categories with depth. For PFe attenuation, + and – denote the magnitude of the decrease or
431 increase in the flux with depth, respectively. Note, the dynamic nature of concurrent ligand
432 release and scavenging as particles settle, means that $L^* > 0$ may not impede scavenging (see
433 Fig. 3c). Nevertheless, the higher the value of L^* the less likelihood of pronounced
434 scavenging.

435

436 **Figure 5. Results of model simulations using lithogenic particle-dependent modulation of**
437 **iron remineralization. a,** Relationship between R_{Fe/O_2} and lithogenic PFe concentrations in
438 offshore regions (>3000 m depth; 30°S-30°N) employing different lithogenic particle-
439 dependent modulators of iron remineralization (kd; Methods). **b,** Change in DFe inventory
440 vertically integrated over 100-250 m (upper-panel) and 1000-1250 m (lower-panel) depth
441 strata relative to the control run. This simulation is based on a 500-year simulation employing
442 a kd of $0.1 \mu\text{g m}^{-3}$ (i.e., which reproduced the inverse relationship observed between R_{Fe/O_2}
443 and the lithogenic PFe concentration in panel a). **c,** Alteration of the global mean vertical DFe
444 profile from a simulation employing a kd of $0.1 \mu\text{g m}^{-3}$ relative to the control run.

445

446 **METHODS**

447 **Site selection** – Datasets were acquired during two GEOTRACES process studies, in the
448 Subantarctic Zone (SAZ) southwest of Tasmania, aboard the *RV Investigator* (March 2017;
449 SOTS project), and in the central (Ionian Sea, ION) and western (Algerian Basin, ALG)
450 Mediterranean Sea aboard the *RV Pourquoi Pas?* (May/June 2017; Peacetime project). Sites
451 were selected for their contrasting magnitude and composition of the downward particle flux.
452 In particular, ~30-fold higher lithogenic fluxes have been reported at ~1000 m depth at ALG
453 ($12.7 \text{ g m}^{-2} \text{ yr}^{-1}$)³⁶ and ION ($13.9 \text{ g m}^{-2} \text{ yr}^{-1}$)³⁷, relative to SAZ ($0.4 \text{ g m}^{-2} \text{ yr}^{-1}$)²⁷. In contrast,
454 POC fluxes at ~1000 m depth are relatively similar at SAZ ($1.1\text{-}1.4 \text{ g m}^{-2} \text{ yr}^{-1}$)³⁸, ALG (1.4-
455 $1.7 \text{ g m}^{-2} \text{ yr}^{-1}$)³⁶, and ION ($0.7\text{-}0.9 \text{ g m}^{-2} \text{ yr}^{-1}$)³⁷.

456 The SAZ represents >50% of the areal extent of the ice-free Southern Ocean. This HNLC
457 area has both low silicate and DFe concentrations year round²⁴ along with moderate
458 phytoplankton biomass³⁹. The low dust flux to this area originates primarily from Australia,
459 with the highest fluxes between October and March⁴⁰. POC ($0.91\text{-}1.23 \text{ mmol m}^{-2} \text{ d}^{-1}$) and PFe
460 ($0.48\text{-}0.67 \text{ } \mu\text{mol m}^{-2} \text{ d}^{-1}$) fluxes measured in this study compared well with POC (3.34 ± 1.81
461 $\text{mmol m}^{-2} \text{ d}^{-1}$)⁴¹ and PFe ($0.17 \pm 0.09 \text{ } \mu\text{mol m}^{-2} \text{ d}^{-1}$)⁴² fluxes measured at the same site and
462 depth, but in January/February.

463 The Mediterranean Sea has a west-to-east gradient of increasing oligotrophy, with a
464 deficiency of phosphorus and nitrogen. Relatively weak winter convection⁴³ prevents efficient
465 uplift of nutrients to the surface waters. Deposition of Saharan desert dust, characterized by
466 strong variability and dominated by extreme events⁴⁴, constitutes the main source of new
467 nutrients. ION is an ultra-oligotrophic area, while the ALG is one of the most productive
468 areas in the Mediterranean Sea⁴⁵. At ALG/ION, POC fluxes measured at 195 m depth (1.14-
469 $1.67 \text{ mmol m}^{-2} \text{ d}^{-1}$) are consistent with previous measurements ($0.4\text{-}3.0 \text{ mmol m}^{-2} \text{ d}^{-1}$, 1st/3rd
470 quartiles)⁴⁶, but ~4-fold higher than fluxes simultaneously measured at 250 m depth with a

471 PPS5 sediment trap (0.32-0.37 mmol m⁻² d⁻¹; N. Leblond, pers. comm.). Similarly, 2-fold
472 higher PFe fluxes were collected at 195 m depth with the TM-RESPIRE (13.4-16.1 μmol m⁻²
473 d⁻¹) compared to PFe fluxes at 250 m depth (PPS5; 4.5-8.5 μmol m⁻² d⁻¹; N. Leblond, pers.
474 comm.).

475

476 **(TM-)RESPIRE** – The conceptual view, functioning and potential artefacts of the RESPIRE
477 particle interceptor are detailed in ref.²². TM-RESPIRE, a trace metal-clean version of
478 RESPIRE, was developed to quantify PFe remineralization rates. TM-RESPIRE is
479 constructed from polycarbonate (PC) except for the PVC indented rotating sphere (IRS), and
480 has identical dimensions to RESPIRE (Supplementary-Fig. 1). The IRS excludes
481 mesozooplankton from the incubation chamber, and delivers particles every ~10 min into this
482 chamber. When the IRS is not rotating, the chamber beneath it is completely closed, avoiding
483 any exchange with the upper part of TM-RESPIRE. Trace metal cleanliness and optode-based
484 oxygen measurements are not reconcilable since plastic material essential for trace elements
485 studies often have high oxygen permeability, and optodes require a metal window. To
486 circumvent these issues, TM-RESPIRE was systematically deployed concurrently with the
487 RESPIRE fitted with an Aanderaa 3830 oxygen optode (resolution < 1 μM; accuracy < 5
488 μM).

489 Optodes were post-calibrated using the Winkler method, and oxygen time-series were
490 corrected for pressure and salinity (Aanderaa operating manual). A pressure sensor (RBR,
491 Canada) was deployed alongside RESPIRE to determine the deployment depth. The vertical
492 distance between the TM-RESPIRE and RESPIRE (10-20 m; Supplementary-Table 1) was
493 constrained by the ship's dimensions (i.e., distance above the waterline) and the necessity to
494 keep a minimum distance between the two traps to avoid contamination through contact with
495 the vessels' hull or propeller wash during deployment/recovery.

496 Remineralization rates measured within the RESPIRE were assumed to be comparable in the
497 TM-RESPIRE. This assumption is supported by similar rates obtained at SAZ after two
498 successive deployments several days apart ($5.1 \pm 0.2 \text{ mmol O}_2 \text{ m}^{-3} \text{ d}^{-1}$; Fig. 3a), and by
499 previous replicate RESPIRE measurements exhibiting small variability in the remineralization
500 rates⁴⁷. In the present study, POC fluxes from RESPIRE and TM-RESPIRE (vertically
501 separated by 10-20 m) varied on average by a factor of 1.8 ± 0.6 ($n = 6$). Similar POC flux
502 variabilities were observed at ALG/ION (250 m depth) and SAZ (150 m depth) across
503 individual 12-24 h samples obtained by conventional sediment traps which varied on average
504 by 1.6 ± 0.8 (N. Leblond, pers. comm.) and $3^{(41)}$, respectively. This relatively high variability
505 in successive upper mesopelagic POC flux measurements suggests that the differences
506 observed in the present study is driven largely by inherent variability in the POC flux in this
507 stratum⁴⁸, rather than by the vertical spacing between the RESPIRE and TM-RESPIRE.

508

509 **(TM-)RESPIRE procedure** – RESPIRE were cleaned following ref.²². Before each voyage,
510 TM-RESPIRE were soaked in 2% Neutracon (7d), 2 M HCl (reagent grade; 30d), 1.2 M HCl
511 (TM grade; 7d), and copiously rinsed with Ultrapure water. Before deployment, each TM-
512 RESPIRE was filled overnight with 0.12 M HCl (TM grade), rinsed with Ultrapure water and
513 pre-conditioned with low-Fe filtered seawater to remove all trace of acid. Several hours
514 before deployment, RESPIRE and TM-RESPIRE were filled with filtered seawater collected
515 at the deployment depth. Clean polyethylene (PE) bags covering the traps were removed just
516 prior to deployment. Upon recovery, RESPIRE and TM-RESPIRE were immediately covered
517 with PE bags. TM-RESPIRE's were transferred into a class-100 clean laboratory. Seawater
518 above the IRS was siphoned off using clean Teflon PFA tubing, and the incubation chamber
519 was sampled via a Teflon PFA stopcock valve. The absence of mesozooplankton in the
520 chamber was confirmed by visual inspection. Samples were split into equal fractions and

521 subsamples for DFe, Fe-binding ligands, and nutrients were filtered through acid-cleaned 0.2-
522 μm PC membranes. DFe samples were stored in low density PE (LDPE) bottles and acidified
523 to pH 1.8 (quartz-distilled HCl). Fe-binding ligand samples were transferred to high density
524 PE bottles (cleaned following GEOTRACES protocols,
525 [http://www.geotraces.org/science/science-highlight/intercalibration/222-sampling-and-](http://www.geotraces.org/science/science-highlight/intercalibration/222-sampling-and-sample-handling-protocols-for-geotraces-cruises)
526 [sample-handling-protocols-for-geotraces-cruises](http://www.geotraces.org/science/science-highlight/intercalibration/222-sampling-and-sample-handling-protocols-for-geotraces-cruises)), double-bagged and stored at -20°C . 0.2- μm
527 PC membranes were dried under a laminar flow hood and used for particulate trace element
528 analysis. Subsamples for POC were obtained by filtration onto pre-combusted 13-mm QMA
529 or GF/F filters. RESPIRE was sampled for POC and nutrients. All steps were performed
530 within 2-3 hours of recovery of (TM-)RESPIRE.
531 TM-RESPIRE procedural blank measurements were performed onboard during voyages.
532 Blanks comprised incubating $<0.2\text{-}\mu\text{m}$ seawater from 150 m depth within the TM-RESPIRE.
533 After 72 h, the blank samples were subjected to identical processing protocols (i.e.,
534 subsampling, filtration) as for deployments. The average DFe blank ($\text{DFe}_{\text{blank}}$; 0.38 ± 0.03
535 nM) was used to correct DFe release (see Calculation of metrics). However, we acknowledge
536 that deployment and recovery are two steps with high risk of contamination. Concentrations
537 in trace elements other than Fe (such as Zn) measured within the TM-RESPIRE were used to
538 assess possible contamination (not necessarily conspicuous with DFe) that could have
539 occurred during deployment/recovery. This approach allowed us to reject one contaminated
540 deployment (Subantarctic voyage, April 2016).

541

542 **Water column sampling** – Samples were collected using a Titanium Rosette mounted with
543 Teflon-coated 12 L Niskin (SAZ) or Go-Flo bottles (ALG/ION) deployed on a Kevlar cable.
544 After recovery, bottles were transferred inside a class-100 clean laboratory container.
545 Seawater samples were directly filtered from the bottles through acid-cleaned 0.2- μm capsule

546 filters (Sartorius Sartobran-P-capsule 0.45/0.2- μm). DFe samples were stored in LDPE bottles
547 and acidified to pH 1.8 (quartz-distilled HCl), while nutrient samples were analyzed at sea.
548 Suspended particulate trace elements were sampled using in situ pumps (McLane; acid-
549 cleaned 1- μm PC membranes) at SAZ and pressurized Go-Flo bottles at ALG/ION (acid-
550 cleaned 25-mm diameter Supor 0.45- μm polyethersulfone filters; 4.8 L on average) following
551 GEOTRACES recommendations.

552

553 **Analytical methods** – DFe concentrations were measured by flow injection with online
554 preconcentration and chemiluminescence detection^{3,49}. An internal acidified seawater
555 standard was measured daily to control the stability of the analysis. During the analysis of
556 TM-RESPIRE and water-column samples, the detection limit was 15 pM and the accuracy of
557 the method was controlled by analyzing the SAFe S (0.086 ± 0.010 nmol/kg ($n = 3$);
558 consensus value 0.093 ± 0.008 nmol/kg), SAFe D1 (0.64 ± 0.13 nmol/kg ($n = 19$); consensus
559 value 0.67 ± 0.04 nmol/kg), GD (1.04 ± 0.10 nmol/kg ($n = 10$); consensus value 1.00 ± 0.10
560 nmol/kg), and GSC (1.37 ± 0.16 nmol/kg ($n = 4$); consensus value not available) seawater
561 standards.

562 Dissolved nutrients were analysed onboard with a segmented flow analyser (AAIII HR Seal
563 Analytical; detection limits were 0.02 μM for P, 0.05 μM for N, and 0.08 μM for Si)^{50,51}.

564 Iron organic speciation measurements were performed using CLE-CSV with 2-(2-
565 Thiazolylazo)-p-cresol (TAC) as the competing ligand⁵². Reagent blanks for Fe were
566 undetectable and the detection limit for ligand concentrations was calculated as 3 times the
567 standard deviation of the concentrations (ranging from 0.09-0.99 nM and always lower than
568 the concentration).

569 Particulate trace element samples were digested (10% HF/50% HNO₃ (v/v)) following the
570 protocol described in the “GEOTRACES Cookbook” and ref.⁵³. Procedural blanks consisted

571 of unused acid-cleaned filters. Analyses were performed on a high resolution ICP-MS
572 (Element XR, Thermo-Fisher Scientific). The accuracy of the measurements was established
573 using a range of Certified Reference Materials, including MESS-4. The recoveries in these
574 reference materials were 80-130% for iron.

575 POC samples were acidified overnight with 2 M HCl to remove inorganic C, and then dried at
576 60°C for 2 d. Samples were analyzed on a CHN analyser (Thermo Finnigan EA 1112 Series
577 Flash Elemental Analyser).

578

579 **Calculations of metrics** – Mesozooplankton, free-living and particle-attached heterotrophic
580 bacteria drive mesopelagic remineralization⁵⁴. By excluding mesozooplankton (using the IRS)
581 and boosting particle-attached bacterial abundances relative to free-living bacteria (through
582 particle interception), the measured remineralization rates were dominated by the particle-
583 attached microbial assemblage²².

584 **Particle remineralization** was calculated as follows: the pre-incubation O₂ concentration
585 (Fig. 1b) was subtracted from each data-point obtained during the incubation, and the sign
586 reversed. The slope of the linear regression between this remineralization signature and the
587 time elapsed corresponds to the particle remineralization rate. Note that the decrease in O₂
588 was not systematically linear, and a plateau can be attained toward the end of the incubation
589 (Fig. 1b). The explanation for this trend remains unclear, but may be related to particle
590 containment, a shift in the microbial community⁵⁵, and/or altered organic matter lability²².
591 When such a plateau was evident, remineralization was calculated over the time period where
592 the decrease in O₂ was maximum (Fig. 1b). Since remineralization rates were assumed to be
593 comparable within the RESPIRE and TM-RESPIRE, the error in remineralization rates was
594 calculated by propagating the uncertainty from the slope of the linear regression and the
595 relative standard deviation of the POC fluxes collected by the RESPIRE/TM-RESPIRE. The

596 error in ΔO_2 (see below) was calculated in the same way.

597 **The iron regeneration efficiency** (R_{Fe/O_2} ; $\mu\text{mol}/\text{mol}$; Fig. 3b) was calculated as: $R_{Fe/O_2} =$
598 $\Delta\text{DFe} / \Delta O_2$, where $\Delta\text{DFe} = \text{DFe}_{\text{post-incubation}} - (\text{DFe}_{\text{initial}} + \text{DFe}_{\text{blank}})$, and $\Delta O_2 = O_{2\text{ pre-incubation}} -$
599 $O_{2\text{ post-incubation}}$ (initial, pre-incubation, and post-incubation terms are illustrated in Fig. 1a). The
600 error in R_{Fe/O_2} was calculated by propagating the uncertainties from ΔDFe and ΔO_2 .

601 **The Fe/C regeneration ratio** ($R_{Fe/C}$; $\mu\text{mol}/\text{mol}$; Fig. 3c) was calculated as: $R_{Fe/C} = R_{Fe/O_2} /$
602 0.69 , where 0.69 is a C: O_2 conversion factor (i.e., $117/170$)⁵⁶. Note that different conversion
603 factors can be used to convert the oxygen-based remineralization rate to carbon (discussed in
604 detail in ref.²²).

605 **Particulate fluxes were expressed as concentrations** to permit cross-comparison between
606 sites in which different collection times were employed (Supplementary-Table 1). **Pre-**
607 **incubation particulate Fe, P, and OC concentrations** correspond to the sum of the post-
608 incubation particulate concentration, plus the concentration of the respective element released
609 into the dissolved phase (i.e., ΔDFe , $\Delta\text{PO}_4 (= \text{PO}_4_{\text{post-incubation}} - \text{PO}_4_{\text{initial}})$, and $\Delta\text{OC} (= \Delta O_2 \times$
610 $0.69)$, respectively).

611 **The replenishment rate of Fe** ($\% \text{d}^{-1}$; Supplementary-Table 2) was calculated as: $(\Delta\text{DFe} /$
612 $\text{PFe}_{\text{pre-incubation}}) \times 100 / \Delta t$, (Δt corresponds to the incubation time). The error was calculated
613 by propagating the uncertainties from ΔDFe and $\text{PFe}_{\text{pre-incubation}}$. P and C replenishment rates
614 were calculated in the same way.

615 **Quantification of the lithogenic and biogenic fractions of sinking PFe** has large
616 uncertainties. Twining et al.¹⁵ reported a 2.3 and 4.4-fold increase in the Fe/P and Fe/S (proxy
617 of Fe/C) ratios of sinking diatom by 200 m depth, respectively, highlighting difficulties in
618 estimating the biogenic fraction of sinking PFe from surface cell quotas. An alternative
619 approach is to estimate the lithogenic fraction of PFe by using the Fe/Al ratio. However, the
620 present study encompasses different regions where lithogenic material has different Fe and Al

621 compositions. In addition, dissolution/scavenging of Fe and Al differ during particle
622 settling⁶⁰, altering their pre-depositional Fe/Al ratio. Thus, lithogenic PFe estimated at
623 ALG/ION using a Saharan dust end-member Fe/Al ratio⁵⁹ is systematically higher than total
624 PFe. In contrast, suspended particles collected at ALG/ION had a Fe/Al ratio comparable to
625 the crustal Fe/Al ratio⁵⁸ (Supplementary-Fig. 3). Thus, the crustal Fe/Al molar ratio was used
626 to estimate biogenic and lithogenic PFe components in Fig. 2 and 3c. For the remainder of the
627 study, the PFe/POC molar ratio (hereafter termed Fe/C) of the intercepted particles (Fig. 3)
628 was used as a proxy for the composition of the PFe flux. In using this approach, we consider
629 POC and PFe as proxies of biogenic (algal/detrital) and lithogenic PFe, respectively⁹. This
630 ratio increases when the relative proportion of lithogenic Fe increases, and vice-versa. We
631 acknowledge that the biogenic Fe/C ratio differs between Fe-limited and Fe-replete areas,
632 however, we believe that this approach is relatively robust when considering such contrasting
633 sites.

634

635 **Ancillary biogeochemical information** – Surface chlorophyll-*a* was derived from MODIS-
636 Aqua. The 4 km resolution eight-day composite images were averaged over the 2003-2017
637 period (due to extensive subantarctic cloud-cover) for a 1°x1° box centered at each site. At
638 SAZ, MODIS chlorophyll-*a* concentrations were corrected using an improved regional
639 algorithm⁶¹.

640 Monthly estimates of total (wet + dry) dust deposition annually averaged were obtained using
641 an atmospheric model (CAM4-BAM, case C4fn)²³ run for 30 years, of which we considered
642 the last 10 years, with a spatial resolution of 0.9°x1.25°.

643

644 **The PISCES biogeochemical model experiment** – PISCES^{62,63} is a relatively complex
645 general ocean circulation and biogeochemistry model with two PFe pools (large and small)

646 characterized by different sinking rates, and two analogous POC size classes sourced from the
647 ‘mortality’ of organic Fe and C pools. Uncomplexed DFe is subjected to scavenging, while
648 colloidal iron undergoes coagulation losses, both of which augment two PFe size classes.
649 Scavenging rate depends on the particle abundance, including the lithogenic PFe pool (based
650 on the dust input at the surface and a simple sinking speed). Subsurface dissolution of
651 lithogenic PFe occurs with a ~500 m length-scale, a sinking rate of 2 m d^{-1} , and a reduced
652 solubility. PFe remineralization takes into account changes in particle size and lability due to
653 bacterial solubilization via reactivity continuum⁶⁴.

654 We conducted a range of different simulations with PISCES aimed at addressing the first-
655 order influence of lithogenic particles (i.e., dust) on R_{Fe/O_2} . Building this parameterization on
656 dust has many advantages. Indeed, biogenic Fe is a complex pool (detritus/algal)
657 characterized by different cell quotas⁶⁵, while dust supply is a well-established component⁴
658 that does not require explicit modelling of extra pools and can be incorporated more widely
659 into models. In the model, R_{Fe/O_2} is derived by dividing the annually integrated
660 remineralization flux of iron from PFe by the O_2 consumption during remineralization at each
661 model grid cell. We conducted a set of sensitivity experiments where PFe remineralization
662 was modulated by the lithogenic particle concentration at each model grid cell. This
663 modulator (M , an unitless quantity) is a function of the lithogenic particle concentration: $M =$
664 $1 - [\text{lithogenic particles} / (\text{lithogenic particles} + kd)]$. M has a range of different sensitivities
665 ($kd = 0.1, 1, 5$ and $10 \mu\text{g m}^{-3}$). To avoid double accounting, Fe scavenging by dust included in
666 PISCES⁶² was switched off. We then ran for 500 years experiments as well as a 500-year
667 model run in which PFe remineralization was left unchanged (Supplementary-Fig. 4a). We
668 then compared the range of R_{Fe/O_2} outputs from each experiment with the local lithogenic PFe
669 concentrations (Fig. 5a), which showed that $kd = 0.1 \mu\text{g m}^{-3}$ was the most realistic as it
670 reproduced the inverse relationship observed between R_{Fe/O_2} and the lithogenic PFe

671 concentrations (Fig. 3b). To minimize the impact of high iron inputs (e.g., near shelves), only
672 offshore regions (>3000 m depth; 30°S-30°N) were considered. Finally, the impact of this
673 new parameterization on DFe inventories, vertical DFe distribution, and surface iron-driven
674 processes was investigated.

675

676 **Exploration of caveats** – Our approach comes with some caveats, most of which were
677 identified and discussed in ref.²². Here, we discuss potential biases that may have affected Fe
678 cycling within the TM-RESPIRE. Specifically, we acknowledge that the pre-concentration of
679 particles in a 1.6 L chamber, along with the widely-differing downward fluxes (Fig. 2), may
680 have influenced the DFe replenishment rates.

681 The potential effects of this experimental bias, related to the need of concentrating particles
682 and to the contrasting sites, were tested via *in vitro* incubation experiments (Supplementary-
683 Fig. 5). The rationale, method, and conclusions are described in the Figure caption. Results
684 from these experiments suggest that during the <48 h incubation within the TM-RESPIRE,
685 the limited loss of DFe by adsorption onto walls/particles was not significantly influenced by
686 the particle concentration, and by the surface-area-to-volume (SA:Vol) ratio of the incubation
687 bottles (0.31-0.59 cm⁻¹). This later finding allows us to conclude that a different SA:Vol ratio
688 of the TM-RESPIRE incubation chamber (0.57 cm⁻¹) would not have changed our
689 conclusions.

690 In our study, the concomitant decreases in DFe replenishment and particle volume
691 concentrations observed with depth at ALG/ION (Supplementary-Tables 2 and 4) do not
692 support a particle concentration effect on the replenishment of Fe. This experimental bias, that
693 would act to lower DFe concentration, has mainly been observed during dust dissolution
694 experiments⁶⁶. This effect is likely offset in incubations with mixed biogenic/lithogenic
695 particles (along with the associated bacterial communities) by the concurrent release of Fe-

696 binding ligands (which increased on average by a factor >2 in our study; Supplementary-
697 Table 3). Consistent with the conclusions of this study, the particle composition and/or
698 bacterial communities, rather than experimental parameters, appear to be the primary control
699 of the DFe replenishment rate in these *in vitro* experiments.

700

701 **Data availability** – Modis Chl-a concentrations (ALG and ION sites) were obtained with the
702 Giovanni online data system, developed and maintained by the NASA GES DISC. MODIS
703 Chl-a concentrations corrected using an improved regional algorithm for the Southern Ocean
704 (SAZ site) are publicly available via the Australian Integrated Marine Observing System
705 (IMOS) Ocean Portal (www.imos.org.au). Following publication, the dataset generated and
706 analysed during the current study (mostly available in the Supplementary Information section)
707 will be made available (i.e. open access) through the IMAS/UTAS data portal
708 (<http://www.imas.utas.edu.au/data>).

709

710 **Code availability** – The NEMO-PISCES model we use in this work is freely available
711 (<http://www.nemo-ocean.eu/>) under the CeCILL free software licence
712 (<http://www.cecill.info/index.en.html>). We used a modified version of the PISCES
713 biogeochemical model. These modifications concern the representation of the particulate iron
714 remineralization and this is not yet present in the freely available NEMO release but will be
715 provided upon contacting A.T.

716

717 **References**

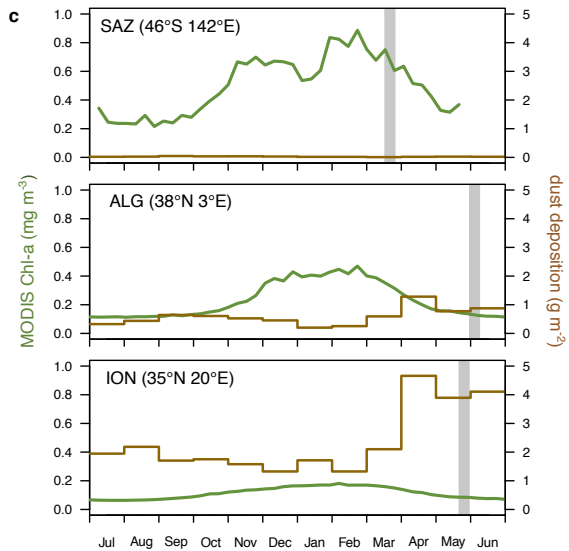
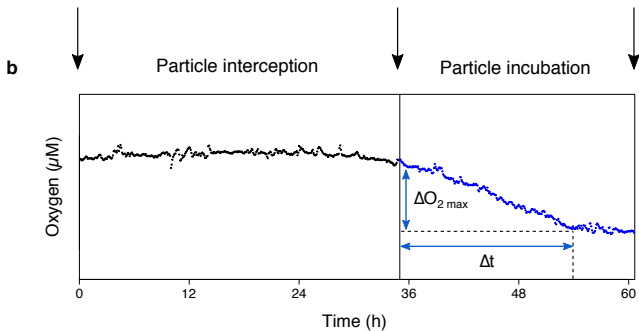
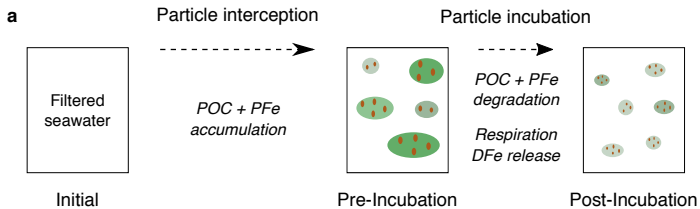
718 36. Zúñiga, D., et al. Particulate organic carbon budget in the open Algero-Balearic Basin
719 (Western Mediterranean): Assessment from a one-year sediment trap experiment. *Deep*
720 *Sea Res. Part I* **54**, 1530-1548 (2007).

- 721 37. Stavrakakis, S., *et al.* Downward fluxes of sinking particulate matter in the deep Ionian
722 Sea (NESTOR site), eastern Mediterranean: seasonal and interannual variability.
723 *Biogeosciences* **10**, 7235 (2013).
- 724 38. Rigual-Hernández, A. S., Trull, T. W., Bray, S. G., & Armand, L. K. The fate of diatom
725 valves in the Subantarctic and Polar Frontal Zones of the Southern Ocean: Sediment trap
726 versus surface sediment assemblages. *Palaeogeogr. Palaeoclimatol. Palaeoecol.* **457**,
727 129-143 (2016).
- 728 39. Eriksen, R., *et al.* Seasonal succession of phytoplankton community structure from
729 autonomous sampling at the Australian Southern Ocean Time Series (SOTS) observatory.
730 *Mar. Ecol. Prog. Ser.* **589**, 13-31 (2018).
- 731 40. Li, F., Ginoux, P., & Ramaswamy, V. Distribution, transport, and deposition of mineral
732 dust in the Southern Ocean and Antarctica: Contribution of major sources. *J. Geophys.*
733 *Res.* **113**, D10207 (2008).
- 734 41. Ebersbach, F., Trull, T. W., Davies, D. M., & Bray, S. G. Controls on mesopelagic
735 particle fluxes in the Sub-Antarctic and Polar Frontal Zones in the Southern Ocean south
736 of Australia in summer—Perspectives from free-drifting sediment traps. *Deep Sea Res.*
737 *Part II* **58**, 2260-2276 (2011).
- 738 42. Bowie, A. R. *et al.* Biogeochemical iron budgets of the Southern Ocean south of
739 Australia: Decoupling of iron and nutrient cycles in the subantarctic zone by the
740 summertime supply. *Glob. Biogeochem. Cycles*, **23**, GB4034 (2009).
- 741 43. D'Ortenzio, F., *et al.* Seasonal variability of the mixed layer depth in the Mediterranean
742 Sea as derived from in situ profiles. *Geophys. Res. Lett.* **32**, L12605 (2005).
- 743 44. Guerzoni, S., *et al.* The role of atmospheric deposition in the biogeochemistry of the
744 Mediterranean Sea. *Progr. Oceanogr.* **44**, 147-190 (1999).

- 745 45. D'Ortenzio, F., & Ribera d'Alcalà, M. On the trophic regimes of the Mediterranean Sea: a
746 satellite analysis. *Biogeosciences* **6**, 139-148 (2009).
- 747 46. Ramondenc, S., et al. An initial carbon export assessment in the Mediterranean Sea based
748 on drifting sediment traps and the Underwater Vision Profiler data sets. *Deep Sea Res.*
749 *Part I* **117**, 107-119 (2016).
- 750 47. McDonnell, A. M., Boyd, P. W., & Buesseler, K. O. Effects of sinking velocities and
751 microbial respiration rates on the attenuation of particulate carbon fluxes through the
752 mesopelagic zone. *Glob. Biogeochem. Cycles* **29**, 175-193 (2015).
- 753 48. Lamborg, C. H., et al. The flux of bio-and lithogenic material associated with sinking
754 particles in the mesopelagic “twilight zone” of the northwest and North Central Pacific
755 Ocean. *Deep Sea Res. Part II* **55**, 1540-1563 (2008).
- 756 49. Bonnet, S., & Guieu, C. Atmospheric forcing on the annual iron cycle in the western
757 Mediterranean Sea: A 1-year survey. *J. Geophys. Res. Oceans* **111**, C09010 (2006).
- 758 50. Rees, C., et al. Methods for reproducible shipboard SFA nutrient measurement using
759 RMNS and automated data processing. *Limnol. Oceanogr. Methods* **17**, 25-41 (2019).
- 760 51. Aminot, A., & Kérouel, R. Dosage automatique des nutriments dans les eaux marines:
761 méthodes en flux continu, Ed. Ifremer, Méthodes d’analyse en milieu marin (2007).
- 762 52. Croot, P. L. & Johansson, M. Determination of Iron Speciation by Cathodic Stripping
763 Voltammetry in Seawater Using the Competing Ligand 2-(2-Thiazolylazo)-p-cresol
764 (TAC). *Electroanalysis* **12**, 565-576 (2000).
- 765 53. Planquette, H., & Sherrell, R. M. Sampling for particulate trace element determination
766 using water sampling bottles: methodology and comparison to in situ pumps. *Limnol.*
767 *Oceanogr. Methods* **10**, 367-388 (2012).
- 768 54. Steinberg, D. K., et al. Bacterial vs. zooplankton control of sinking particle flux in the
769 ocean's twilight zone. *Limnol. Oceanogr.* **53**, 1327-1338 (2008).

- 770 55. LeClerc, G. R., DeBruyn, J. M., Maas, E. W., Boyd, P. W., & Wilhelm, S. W. Temporal
771 changes in particle-associated microbial communities after interception by nonlethal
772 sediment traps. *FEMS microbiol. Ecol.* **87**, 153-163 (2014).
- 773 56. Anderson, L. A., & Sarmiento, J. L. Redfield ratios of remineralization determined by
774 nutrient data analysis. *Glob. Biogeochem. Cycles* **8**, 65-80 (1994).
- 775 57. Reinthaler, T., *et al.* Prokaryotic respiration and production in the meso-and bathypelagic
776 realm of the eastern and western North Atlantic basin. *Limnol. Oceanogr.* **51**, 1262-1273
777 (2006).
- 778 58. Wedepohl, K. H. The composition of the continental crust. *Geochim. Cosmochim. Acta*
779 **59**, 1217-1232 (1995).
- 780 59. Guieu, C., Loye-Pilot, M. D., Ridame, C., & Thomas, C. Chemical characterization of the
781 Saharan dust end-member: Some biogeochemical implications for the western
782 Mediterranean Sea. *J. Geophys. Res.* **107**, ACH-5 (2002).
- 783 60. Baker, A. R., Adams, C., Bell, T. G., Jickells, T. D., & Ganzeveld, L. Estimation of
784 atmospheric nutrient inputs to the Atlantic Ocean from 50° N to 50° S based on large-
785 scale field sampling: Iron and other dust-associated elements. *Glob. Biogeochem. Cycles* **27**,
786 755-767 (2013).
- 787 61. Johnson, R., Strutton, P. G., Wright, S. W., McMinn, A., & Meiners, K. M. Three
788 improved satellite chlorophyll algorithms for the Southern Ocean. *J. Geophys. Res.* **118**,
789 3694-3703 (2013).
- 790 62. Aumont, O., Ethé, C., Tagliabue, A., Bopp, L., & Gehlen M. PISCES-v2: an ocean
791 biogeochemical model for carbon and ecosystem studies, *Geoscientific Model*
792 *Development*, **8**, 2465-2513 (2015).
- 793 63. Völker, C., & Tagliabue, A. Modeling organic iron-binding ligands in a three-dimensional
794 biogeochemical ocean model, *Mar. Chem.*, **173**, 67-77 (2015).

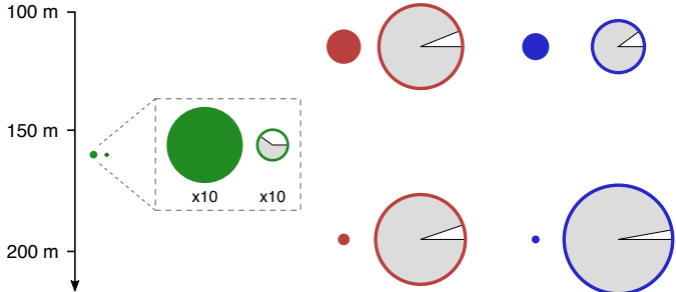
- 795 64. Aumont, O., *et al.* Variable reactivity of particulate organic matter in a global ocean
796 biogeochemical model, *Biogeosciences*, **14**, 2321-2341 (2017).
- 797 65. Boyd, P. W. *et al.* Why are biotic iron pools uniform across high-and low-iron pelagic
798 ecosystems?. *Glob. Biogeochem. Cycles* **29**, 1028-1043 (2015).
- 799 66. Bonnet, S., & Guieu, C. Dissolution of atmospheric iron in seawater. *Geophys. Res. Lett.*
800 **31**, L03303 (2004).

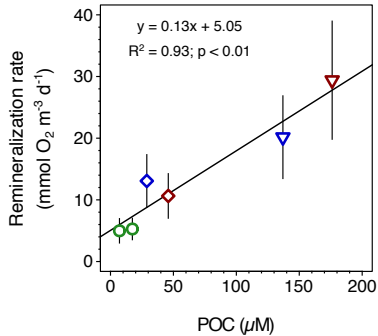
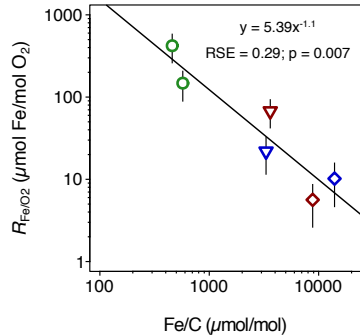
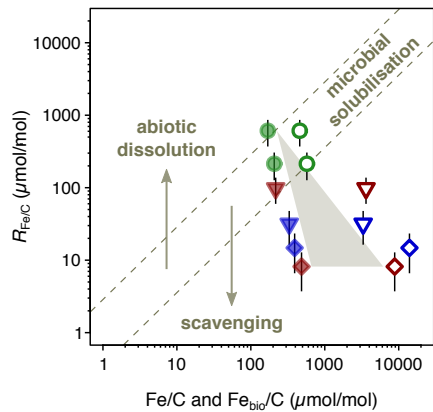


SAZ

ALG

ION



a**b****c**



Biogenic



Mixed



Lithogenic

SAZ

ALG
115 m



ALG
195 m

ION
115-195 m

DFe release
($\mu\text{mol Fe/mol O}_2$)

150-420

68



6

22-10

DFe_{litho}⁽¹⁾
(% of ΔDFe)

0.01%

0.5%



17%

2-9%

Post-incubation L*⁽²⁾

0.43

0.25



0.18

0.21-0.12

Potential lithogenic
scavenging⁽³⁾ (% of ΔDFe)

0.3%

5%



170%

30-130%

PFe attenuation⁽⁴⁾

(+++)

(-)

(- - -)

(1) Estimates based on a dissolution rate of $0.018 \text{ nmol mg}^{-1} \text{ dust d}^{-1(30)}$

(2) L* corresponds to the excess of ligands over DFe after the incubation phase

(3) Estimates based on a scavenging ratio of DFe on dust of $0.37 \text{ nmol mg}^{-1(18)}$

(4) At SAZ, estimate based on the balance between DFe/L release and scavenging

